TUDelft

Delft University of Technology

Adjoint-based optimisation of rocket engine turbine blades

Sanghera, B.S.; Anand, N.; Souverein, Louis; Penin,, Loïc; Pini, M.

Citation (APA)
Sanghera, B. S., Anand, N., Souverein, L., Penin, L., & Pini, M. (2021). Adjoint-based optimisation of rocket engine turbine blades. In *Turbo Expo 2021: Virtual, Online, Virtual Conference and Exhibition* (pp. 1-12). Article GT2021-59580 ASME.

Important note
To cite this publication, please use the final published version (if applicable).
Please check the document version above.

GT2021-59580

ADJOINT-BASED OPTIMISATION OF ROCKET ENGINE TURBINE BLADES

Bhupinder Singh Sanghera, Nitish Anand,
Propulsion & Power,
Faculty of Aerospace Engineering,
Delft University of Technology,
The Netherlands.

Louis Souverein,
ArianeGroup GmbH,
München, Germany

Loïc Penin,
ArianeGroup SAS,
Vernon, France

Matteo Pini,
Propulsion & Power,
Faculty of Aerospace Engineering,
Delft University of Technology,
The Netherlands.

ABSTRACT

Axial turbine stages for gas generator cycle type rocket engines typically employ highly-loaded supersonic stator vanes. Consequently, the flow pattern downstream of the vanes is characterized by shock waves which induce high-frequency excitation on the subsequent rotor. For this reason, the optimal design of the stator is crucial in the context of development of the next generation of high-performance rocket engines, where reusability is a principal design criterion. A thorough comprehension of the loss mechanisms combined with the adoption of automated optimisation techniques can therefore enable new stator designs that may provide large benefits in terms of overall turbine performance and lifespan.

The scope of this study stems from these considerations and its objective is twofold, namely i) the shape optimisation of a supersonic stator for rocket engines and ii) the investigation of the loss mechanisms in supersonic axial turbine stator vanes at on- and off-design conditions. The investigation is performed on stator vanes that are under development for the first turbine stage of a gas generator cycle type rocket engine. The stator vanes are therefore optimised in order to reduce the profile losses by exploiting a novel adjoint optimisation framework for turbomachinery implemented in the open-source code SU2. The effect
on the resulting flow field and loss sources is finally investigated.

Results show that entropy based loss coefficient gains of 6% can be achieved via shape optimisation and that the fluid-dynamic performance of these vanes is less sensitive to changes in pressure ratio compared to the performance provided by the baseline configuration. Eventually, shock-waves remain the primary loss source.

1 Introduction

Since the 1960s, turbines play a pivotal role in driving the turbopump of large rocket engines powering the space exploration program. Turbines employed in rocket engines drive the turbopump that forces the propellants into the high pressure combustion chamber. The key requirements of such a turbine are high power density, light weight and compact size, combined with the capability to handle very high pressure ratios at acceptable efficiency. Because of that, the turbines are typically of axial configuration, constituted by a single or double stage, and the flow in either the stator and rotor passages is highly supersonic. A typical turbine powering the turbopump operates with pressure ratios of the order of $\sim$20 [1].

The stationary vanes of rocket engine turbines are a signif-

icant source of fluid dynamic losses. This is because a typical rocket engine turbine configuration consists of a highly loaded stator vane and an impulse rotor. In such a turbine configuration majority of the expansion process occurs in the stationary vanes, while, the rotor extracts the kinetic energy by turning the flow through its distinctive bucket shape blades. Due to the high load, the stator is bound to operate with the occurrence of shockwave in the blade passage all along the operating envelope of the turbine. Additionally, these shocks make the flow highly non-uniform downstream of the rotor, thus penalizing the overall efficiency of the component. Furthermore, the dynamic excitation induced by the highly non-uniform flow of the rotor blade can lead to cyclic loading and forced response, with the risk of inducing premature structural failure due to high cycle fatigue.

Improving the fluid dynamic performance of the stationary vanes of supersonic turbines can drastically improve the turbine efficiency and life-span and, consequently, can lead to substantial gain in payload performance (€/kg) of space launches. In addition, this could also enable re-usability of the turbine components for subsequent launches. The detrimental impact that the performance of stationary vanes can have on the entire mission makes them an essential component of the rocket engines.

The fluid dynamic design of supersonic stator vanes is particularly challenging, because the blade must be profiled such as to concurrently provide the right turning to the supersonic flow and to withstand the high mechanical loads. A common method to design supersonic blading is the Method of Characteristics (MoC), widely employed for the design of Curtis turbines [2], turbines for pressure gain combustion [3], and of organic Rankine cycle turbines [4]. Despite being an extremely efficient method, it is barely applicable in the context of rocket engine turbine vanes due to the constrains imposed by tight geometrical requirement and employed manufacturing techniques, which would not allow the designer to accommodate the geometry of the diverging section obtained by MoC in the blade shape layout. Therefore, the baseline shape is typically obtained by resorting to engineering best practices based on proprietary knowledge. Especially in this frame, automated CFD-based design can be effectively exploited to redesign the baseline configuration, while accounting for the many manufacturing constraints. Automated CFD-based design methods have been successfully adopted to re-design vanes of organic Rankine cycles (ORC) turbines. For example in Ref. [5], a NURBS-based parameterization technique is used to optimize the supersonic vanes of a radial turbine in combination with a gradient free method. Similarly, in Ref. [6] the authors exploited a free-from deformation surface parametrization method to optimize the supersonic vane of an axial ORC turbine. In Ref. [7, 8], the design methods were also extended to deal with manufacturing uncertainties. According to the literature, no research efforts have been made to apply such automated design techniques to optimize the highly constrained supersonic vanes of rocket engine turbines.

This paper documents the application of the design method described in [6] and [9] to the shape optimization of the supersonic stator geometry of a rocket engine turbine. The method is based on free form deformation boxes [10] to parametrise the blade surface and leverages on the capability of the open-source SU2 software to solve the RANS equations of both the flow and adjoint problem [6]. The design study is performed by considering the stator vanes of a 1MN-class gas generator cycle type rocket engine [11] under development as baseline geometry. The design space is limited to deformation of solely the suction side of the blade, so as to ensure the satisfaction of geometrical constraints without the need of explicitly prescribing them in the optimization problem. The objective of the unconstrained optimisation problem is the minimization of the entropy generation loss coefficient. The baseline and the optimised geometry are assessed for fluid dynamic performance, namely fluid-dynamic loss and downstream flow uniformity, at their nominal and off-design conditions.

The paper is structured into 5 sections. In section 2 the adopted adjoint-based optimisation framework and associated numerical schemes is documented. Section 3 provides details of the case study under consideration and reports on the numerical setting of the flow, adjoint and optimisation framework. Section 4 follows, in which the fluid dynamic assessment and findings derived from the loss breakdown study at nominal and off-design conditions are described. Conclusive remarks and perspectives on future research directions are finally drawn.

2 Methodology

In this section the details of the shape optimisation and loss breakdown methods are presented.

2.1 Shape Optimisation Method

The optimisation framework consists of four steps, namely, surface deformation, volume deformation, flow solver and adjoint solver. This method is adopted from the previous work of Ref. [6, 10] and is briefly detailed here for completeness.

The optimisation framework manipulates the design variables $\boldsymbol{\alpha}$ causing a variation of the blade surface $\mathbf{X}_s$ and as such to the objective function J. This process requires three steps, namely, surface deformation, volume deformation and flow solver. The sensitivity of the objective function with respect to the design variables is then computed through the fourth step of the process, namely, the solution of the adjoint problem.

2.1.1 Surface deformation The free-form deformation (FFD) method proposed in Ref. [12] is used to parametrise the blade surface. The blade geometry is defined by means of parametric curves whose control points determine a cartesian lattice encompassing the blade shape. According to the method, the

change of the surface grid can be written as

$$\Delta \mathbf{X}_{\mathrm{s},n}^d = \sum_{j=0}^{\mathrm{q}} \sum_{i=0}^{\mathrm{o}} B_i^{\mathrm{o}}(d_n) B_j^{\mathrm{q}}(g_n) \left(\mathbf{P}_{i,j}^d - \mathbf{P}_{i,j}^{d-1} \right), \qquad (1)$$

where B_i^{o} and B_j^{q} are the i-th and j-th Bernstein polynomials, d_n and g_{n} are the values of the parametric coordinates in which the n-th point of $\mathbf{X}_{\mathrm{s}}$ is mapped. This allows for continuous movement of the design surface through the control lattice $\mathbf{P}_{i,j}$. Thanks to this association, $\mathbf{P}_{i,j}$ can be used as the design variables $\boldsymbol{\alpha}$ of the optimisation problem. The coordinate of the n-th point of the blade surface mesh at the d-th optimisation step is then given by

$$\mathbf{X}_{\mathrm{s},n}^d = \mathbf{X}_{\mathrm{s},n}^{d-1} + \Delta \mathbf{X}_{\mathrm{s},n}^d. \qquad (2)$$

2.1.2 Volume Deformation
The change in the blade surface, $\Delta \mathbf{X}_s^d$, can be imposed on the volume mesh by modelling it as an elastic solid. the equations of linear elasticity, the change of the blade surface can be imposed on the mesh as a Dirichlet boundary according to [13]

$$\mathbf{K} \Delta \mathbf{X}^d = \mathbf{T} \Delta \mathbf{X}_{\mathrm{s}}^d, \qquad (3)$$

where $\mathbf{X}$ is the volume mesh, $\mathbf{K}$ is a stiffness matrix and $\mathbf{T}$ is a projection matrix which re-orders $\Delta \mathbf{X}_s$ in accordance with $\mathbf{X}$. The volume mesh for the d-th optimisation step is then given by

$$\mathbf{X}^d = \mathbf{X}^{d-1} + \Delta \mathbf{X}^d. \qquad (4)$$

Linear elasticity model is capable of handling volume deformation for small displacement values, which is usually the case for shape optimization problems.

2.1.3 Flow Solver
The Reynolds-Averaged Navier-Stokes (RANS) equations are solved using the fixed-point iterator, $\mathbf{G}(\mathbf{U}^n, \mathbf{X})$, that represents the time integration of the equations according to an implicit Euler method, i.e.

$$\mathbf{U}^{n+1} = \mathbf{G}(\mathbf{U}^n, \mathbf{X}). \qquad (5)$$

where $\mathbf{U}$ are the conservative flow variables. It is assumed that $\mathbf{G}$ is stationary only at feasible points $\mathbf{U}^*$,

$$\mathbf{R}(\mathbf{U}^*, \mathbf{X}) = 0 \Leftrightarrow \mathbf{U}^* = \mathbf{G}(\mathbf{U}^*, \mathbf{X}), \qquad (6)$$

where $\mathbf{R}$ is the residual vector obtained from the spatial integration of the governing flow equations.

The flow solver has been validated extensively on relevant turbomachinery test cases, including transonic and supersonic turbines [14].

2.1.4 Adjoint Solver
The minimization problem corresponding to the shape optimisation framework presented can be given as

$$\min_{\boldsymbol{\alpha}} \quad J(\mathbf{U}(\boldsymbol{\alpha}), \mathbf{X}(\boldsymbol{\alpha})), \qquad (7)$$

$$\text{s.t.} \quad \mathbf{U} = \mathbf{G}(\mathbf{U}, \mathbf{X}), \qquad (8)$$

$$\mathbf{X} = \mathbf{M}(\boldsymbol{\alpha}) = \mathbf{V}(\mathbf{S}(\boldsymbol{\alpha})). \qquad (9)$$

where $\mathbf{M}$ is the operator containing the surface and volume deformation. Following the Lagrangian multiplier approach to arrive at the adjoint equation from the optimisation formulation two equation can be obtained. These equations correspond to the flow ($\bar{\mathbf{U}}$) and the mesh ($\bar{\mathbf{X}}$) adjoint variables and is given as

$$\bar{\mathbf{U}} = \frac{\partial}{\partial \mathbf{U}} J^T(\mathbf{U}, \mathbf{X}) + \frac{\partial}{\partial \mathbf{U}} \mathbf{G}^T(\mathbf{U}, \mathbf{X}) \bar{\mathbf{U}}, \qquad (10)$$

$$\bar{\mathbf{X}} = \frac{\partial}{\partial \mathbf{X}} J^T(\mathbf{U}, \mathbf{X}) + \frac{\partial}{\partial \mathbf{X}} \mathbf{G}^T(\mathbf{U}, \mathbf{X}) \bar{\mathbf{U}}. \qquad (11)$$

It can be observed that $\bar{\mathbf{U}}$ has an implicit dependence, see Eqn. (10), and hence needs to be iterated. Meanwhile, $\bar{\mathbf{X}}$ has an explicit dependence, see Eqn. (11) and can be computed directly once $\bar{\mathbf{U}}$ is known.

Following this, the derivative of the objective function with respect to the design variable can be computed as

$$\frac{\mathrm{d}J}{\mathrm{d}\boldsymbol{\alpha}}^T = \frac{\mathrm{d}}{\mathrm{d}\boldsymbol{\alpha}} \mathbf{M}^T(\boldsymbol{\alpha}) \bar{\mathbf{X}}, \qquad (12)$$

The sensitivity of the mesh operator ($\mathbf{M}$) with respect to the design variable ($\boldsymbol{\alpha}$) is obtained by using an algorithmic differentiation (AD) tool CodiPack [15]. This AD tool allows for automatic differentiation of the source code [16].

2.2 Loss Breakdown Method

The two-dimensional fluid-dynamic loss sources are expressed in terms of kinetic energy loss coefficient $\xi \approx 1 - \eta = 1 - h_{\text{out,tot}} - h_{\text{out}}/h_{\text{out,tot}} - h_{\text{out,is}}$, following the procedure described in Ref. [17], where h is the enthalpy, the subscripts 'in' and 'out' refer to the inlet and outlet, and the subscript 'is' refers to isentropic conditions.

The boundary layer loss can be computed in terms of energy loss coefficient by means of the kinetic energy defect of the boundary layer. In the present study, the free-stream conditions are extracted at the edge of the boundary layers at $0.75\, l/l_{\text{max}}$ and $0.9\, l/l_{\text{max}}$ of the pressure and suction surface, respectively, where the curvilinear abscissa l is measured from the leading edge. The final equation for the boundary layer loss can be written as

$$\xi_{\text{bl}} = \frac{0.5\rho_e \delta_{\text{e}} u_e^3}{\dot{m} c_{\text{p}} T_{\text{in,tot}} \left[1 - \left(1 + \frac{\gamma-1}{2} M_{\text{out,is}}^2 \right)^{-1} \right]}. \tag{13}$$

where ρ is the density, δ is the boundary layer thickness, u the velocity, $\dot{m}$ is the mass flow rate, c_p is the specific heat at constant pressure, T is the temperature, γ is the ratio of specific heats, M is the Mach number and the subscript 'e' represents the edge of the boundary layer.

The shock loss is evaluated in terms of the energy loss coefficient by computing the total pressure deficit in the wake-free regions at the downstream boundary. In transonic flows an estimate of the total pressure deficit can be obtained by evaluating the total pressure loss along a streamline which is set to pass through the shocks only, and that is therefore not affected by boundary layers or wake effects. A streamline suited for this type of analysis is the one passing through the center of the throat section. However, this method is not readily applicable to supersonic flows, whereby the strong shocks cause significant deflection of the streamlines, often resulting them to end near or inside the wake region. Therefore, for supersonic flows, it is preferable to estimate the deficit as the difference between the inlet total pressure and the mass-weighted average of the total pressure computed in the wake-free region at the outlet boundary. The average total pressure in the wake-free region can be obtained by averaging the local total pressure values that are higher than the mass-weighted average calculated over the entire outlet boundary. The final equation for the shock loss reads

$$\xi_{sw} = 1 - \frac{1 - \left(\frac{p_{\text{out}}}{p_{\text{out,tot}}} \right)^{\frac{\gamma-1}{\gamma}}}{1 - \left(\frac{p_{\text{out}}}{p_{\text{in,tot}}} \right)^{\frac{\gamma-1}{\gamma}}}. \tag{14}$$
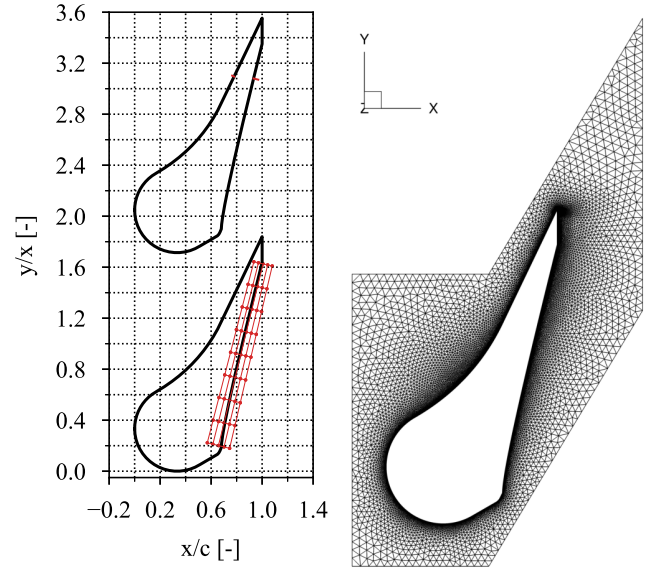

FIGURE 1: Geometry of the supersonic stator vane and the FFD box (left), and the mesh utilised for fluid dynamic simulation (right) in the present study.

The wake-free region obtained using the method described above is shown for the baseline and optimised design under nominal operating conditions in Figure 6 and Figure 7, respectively.

The trailing edge loss is finally computed in terms energy loss coefficient as simply the difference between the total loss, and the individual loss contributions due to the boundary layers and the shocks. The total loss is determined in a similar fashion as the shock loss, but using the mass-weighted average of the total pressure calculated at the downstream plane.

The loss breakdown procedure was validated in Ref. [9] using the transonic LS89 turbine blade with the experimental results documented in Ref. [17]. The numerical loss trends were found to be in agreement with the experimental data and therefore the loss breakdown method is considered suited for the purpose of the present study.

3 Case Study

The optimisation framework is applied to redesign the supersonic stator vane of a 1MN-class gas generator cycle type rocket engine. The operating pressure ratio of this stator is around 20, which is typical for gas generator type rocket engines, see Ref. [1] for more details.

The stator geometry under study and the superimposed FFD box are illustrated in Figure 1. Note that the geometry is not characterized by the traditional converging diverging section, typical of supersonic vanes, but is instead constituted by a predominantly converging flow passage with the sonic throat located close to the pressure side of the trailing edge. The flow domain

4

corresponding to the stator geometry is discretized using an in-house unstructured meshing tool [18]. The hybrid mesh consists of quadrilateral elements close to the blade surface with a y^+ value of unity and triangular elements in rest of the flow domain. The flow solution is obtained by using the RANS solver available in the open-source CFD software SU2 [19]. The turbulence is modeled through two equation $k - \omega$ SST model [20]. The thermodynamic closure is achieved by assuming a calorically perfect gas, which is a valid approximation considering the flow regime typical of these stators. The laminar viscosity is determined using the Sutherland's law and the laminar and turbulent Prandtl number are assumed to be constant and equal to 0.72 and 0.9 respectively.

The calculation is carried out by fixing the total pressure and temperature at the inlet and the accelerating the flow by gradually reducing the back-pressure. The inflow and outflow boundaries are treated with non-reflective boundary conditions to suppress shock-wave reflection from the boundaries [21]. The specifics of the boundary conditions cannot be disclosed due to confidentiality reasons. Temporal integration of the flow governing equations is achieved by using an Euler implicit scheme with a fixed Courant-Friedrichs-Lewy (CFL) number of 10. The convective fluxes are discretised using a second-order accurate classic upwind Roe scheme [22] and spurious oscillations due to shocks and discontinuities are avoided by the van Albada slope limiter [23]. The viscous fluxes are determined using the weighted least square method. The flow solver utilises the matrix-free FGMRES [24] method with the Lower-Upper Symmetric Gauss-Seidel (LUSGS) [25] preconditioner. A maximum of 6000 iterations is set in the flow solver to ensure a residual reduction of 4 orders of magnitude.

The results of the grid convergence study performed are illustrated in Figure 2. The figure shows that a mesh of about 80k cells over predicts the total pressure loss coefficient Y, defined by Eq. (15) [26] by 1% when compared to the finest mesh considered in the present study. Hence, this mesh is deemed sufficiently fine for optimisation purposes. The mesh adopted in the present study has about 80k cells and is depicted in Figure 1.

$$Y = \frac{p_{\text{in,tot}} - p_{\text{out,tot}}}{p_{\text{out,tot}} - p_{\text{out}}}. \qquad (15)$$

The design problem is formulated in terms of the minimization of the objective function and can be mathematically represented as

$$\min_{\boldsymbol{\alpha}} \quad J(\boldsymbol{\alpha}) = \xi_s(\boldsymbol{\alpha}), \qquad (16)$$
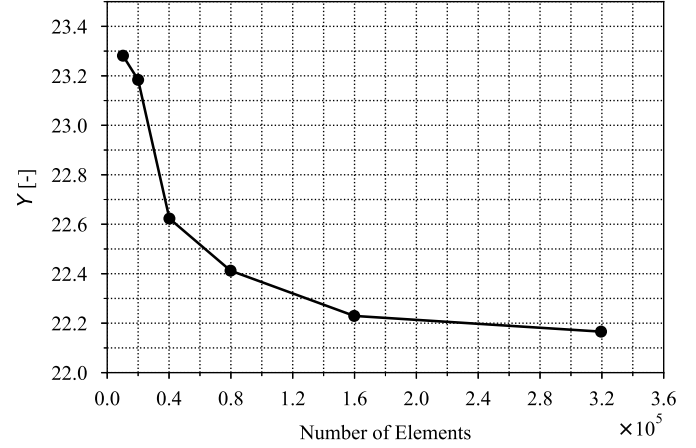

FIGURE 2: Sensitivity of the mesh density on loss coefficient Y.

where the entropy loss coefficient ξ_s is defined as

$$\xi_s = T_{\text{in,tot}} \frac{(s_{\text{out}} - s_{\text{in}})}{u_{\text{out,is}}^2}, \qquad (17)$$

where s is entropy, T is temperature, u is isentropic velocity and subscript 'is' stands for isentropic. The thermodynamic quantities at the inlet ('in') and outlet ('out') boundaries are obtained using the mixed-out averaging method. The flow non-uniformity is instead calculated as standard deviation, i.e. σ_A, with respect to the mean static pressure along the outlet boundary, and is defined as

$$\sigma_A(p) = \sqrt{\frac{\sum_{n=1}^{N} y_i (p_i - \bar{p})}{\sum_{n=1}^{N} y_i}} \qquad (18)$$

where N is the total number of weights and y_i is the i-th pitchwise increment length at the outlet plane.

The FFD box defined in the current study consists of 9 degrees in the jth direction and 5 in the ith direction, see Figure 1. This makes the design variable vector $\boldsymbol{\alpha}$ of size 45, consisting of all the lattice points in the FFD box that can be moved in both $x-$ and $y-$direction. It can be seen from Figure 1 that the FFD box is restricted to the supersonic suction side of the stator vane, namely the throat and trailing edge cannot be deformed. This is owing to (i) indirectly satisfy manufacturing and thermomechanical constraints on the trailing edge thickness and to (ii) fix the mass flow rate to the nominal value without resorting to a constrained optimisation method.

The optimisation problem is solved by means of the gradient-based Sequential Least Squares Programming (SLSQP)
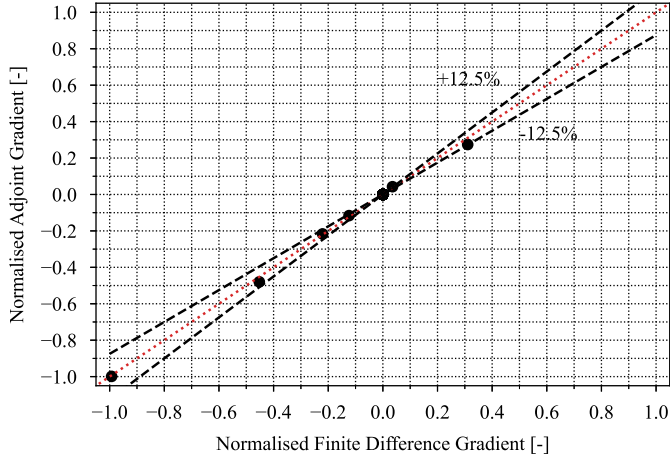
FIGURE 3: Adjoint-based sensitivities vs finite-difference sensitivities. The dots represent the non-zero values of the gradient.

FIGURE 4: Optimisation history of normalised entropy generation loss coefficient and outlet pressure non-uniformity parameter.

algorithm, available in the SciPy package of Python. This algorithm is based on the Quasi-Newton method with a Broyden-Fletcher-Goldfarb-Shanno update for the Hessian of the cost function. Convergence of the optimisation is achieved by satisfying the Karush-Kuhn-Tucker (KKT) conditions with a tolerance of 1×10^{-6} and the maximum number of iterations was set to 50. The cost function and its sensitivity information is under-relaxed by a factor 1×10^{-6} to achieve smooth convergence.

4 Results

The gradients of the 45 design variables obtained from the discrete adjoint method were validated with a first-order forward finite difference scheme with a step size of 1×10^{-3}. Figure 3 shows a scatter plot of the gradients of entropy generation obtained using the discrete adjoint and the finite difference method. It can be observed that most of the design points fall on the dotted red line which represents equality between the two gradients, advocating the accuracy of gradients obtained using the adjoint method. In addition, it also indicates that the adjoint equations have converged sufficiently. Note that in Figure 3 the sensitivities with respect to a large number of design variables is nearly zero.

Figure 4 shows the optimisation history and it can be observed that the optimum design was obtained in 49 steps. The optimum design is characterised by a 6% reduction in the objective function. In addition, the pressure non-uniformity parameter, defined as the standard deviation from the area-weighted mean value, at the outlet of the stator, monitored during the run-time of the optimisation, also shows 6% reduction.

The baseline and the obtained optimised vane geometries are illustrated in Figure 5. It can be observed that the optimised geometry features a curved supersonic suction surface with a con-
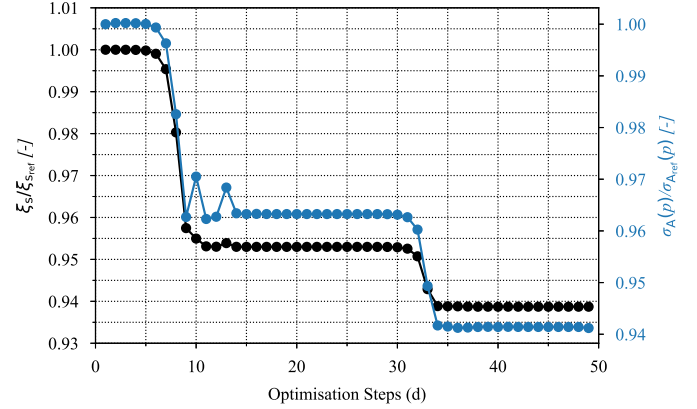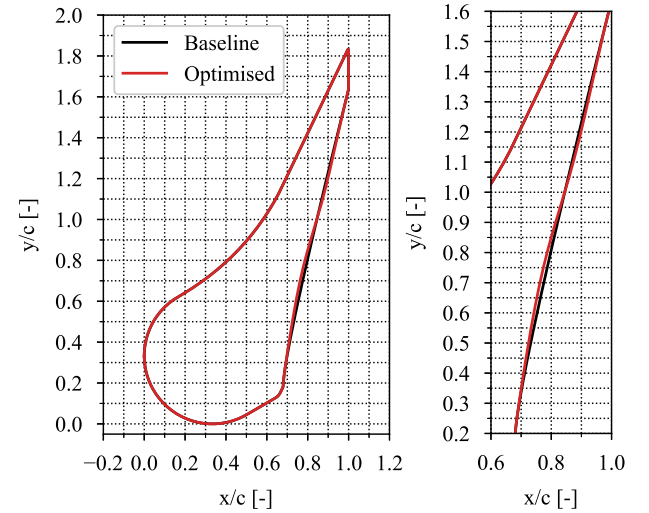

FIGURE 5: Baseline (black) and optimised (red) stator vane geometries.

cave shape between y/c of 0.4-1.0 and a convex shape between y/c of 1.0-1.4. The maximum change between the two geometries is in the order of 4% of the axial chord. The geometry changes are relevant in a real environment and future experimental studies will confirm this statement. The differences between the baseline and optimized profile are also relevant from a manufacturing point of view; they are well within what is feasible with machining methods.

The fluid dynamic assessment of the baseline and the optimised geometry is performed at nominal and part-load operating conditions.
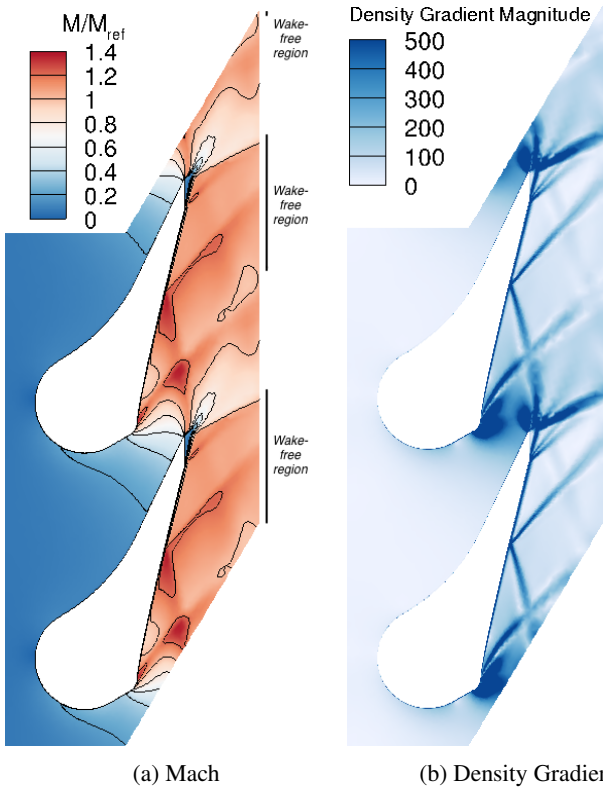
6

(a) Mach   (b) Density Gradient

FIGURE 6: Mach and density gradient contours of the baseline stator vane at nominal operating conditions. The reference value represents the average target value for the outlet Mach number.

(a) Mach   (b) Density Gradient

FIGURE 7: Mach and density magnitude contours of the optimised stator vane at nominal operating conditions. The reference value represents the average target value for the outlet Mach number.

4.1 Nominal Performance

4.1.1 Flow Field Figure 6 illustrates the Mach number and density gradient contour plot for the baseline geometry at nominal operating conditions. Due to the shape of the flow passage being mostly converging, a large part of the expansion occurs in the downstream semi-bladed region, often referred to as post-expansion region. Downstream of the throat, two shock-waves are formed on the blade surface. The shockwave formed at the suction side exits the flow domain, while the one formed at the trailing edge reflects-off of the suction side of the adjacent blade before exiting the flow domain, see Figure 6b. Furthermore, a complex shock-induced flow field can be observed close to the trailing edge of the stator vane. This complexity can be attributed to the blunt trailing edge [27], instead of the conventional rounded one. Its peculiar shape is eventually responsible of the formation of a double fishtail shock pattern interacting with the large wake formed just behind the trailing edge.

Similar contours, i.e. contours of the Mach and density gradient, for the optimized geometry are reported in Figure 7. It can be observed that the shockwave pattern is similar to that obtained for the baseline geometry, except for the shock strength and angle. The strength of the shockwave reflecting off of the
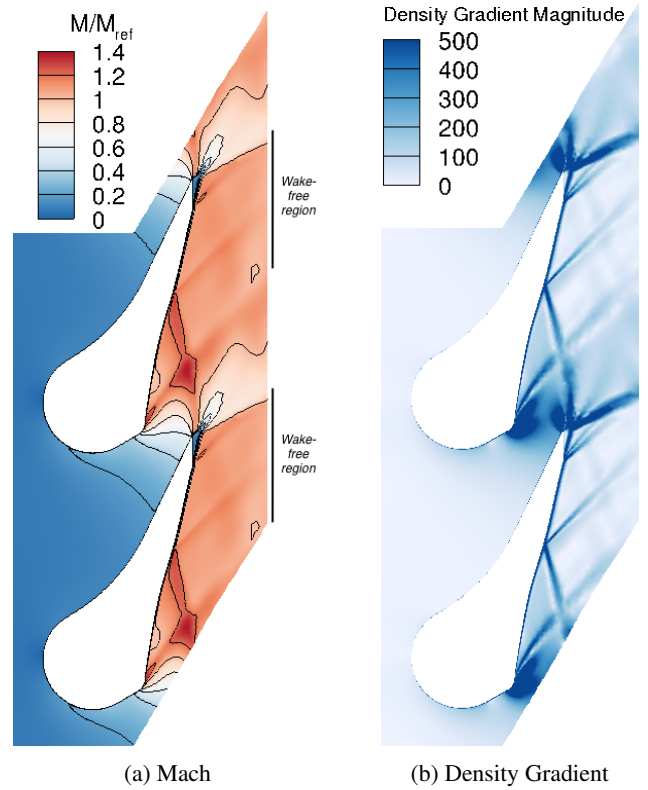
suction side of the blade surface is weaker, see Figure 7b, when compared to that of the baseline geometry, see Figure 6b. This reduction in shock strength can be attributed to the concave shape of the blade surface achieved in optimized blade in section y/c of 0.4-1.0, see Figure 5. This enables a more gradual acceleration of the flow along the wall and, thus, avoids over-expansion. As a consequence, the flow upstream of the shock impingement region is at lower Mach number which leads to a weaker shock-wave originating from the trailing edge and also a weaker reflected shockwave from the suction surface.

This observation can be further substantiated by inspection of the isentropic Mach number distribution along the suction surface downstream of the vane throat, see Figure 8. It can be observed that the Mach number generated before the trailing edge shock impinges on the suction side of the blade is lower in the optimized geometry, see between $l/l_{\max}$ of 0.5-0.7.

4.1.2 Flow Non-Uniformity Another important parameter for efficient turbine performance is the flow uniformity at the exit of the stator vane. This is because a highly non-uniform flow entering the rotor is one of the main cause of the high fluid-
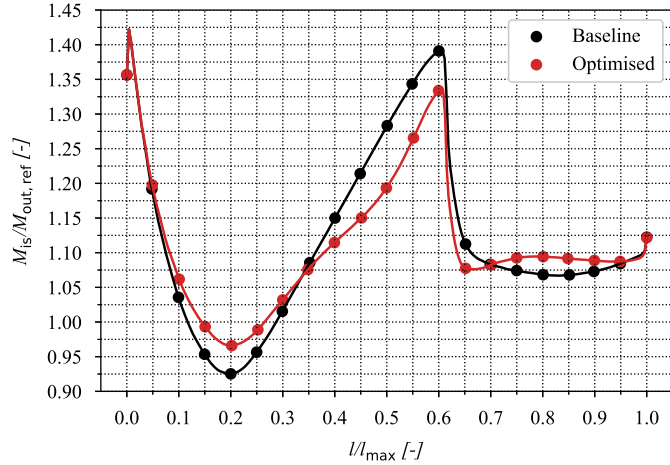
7

FIGURE 8: Isentropic Mach number distribution along the blade suction surface. The curvilinear abscissa l is measured from the throat. The reference value represents the average target value for the outlet Mach number.
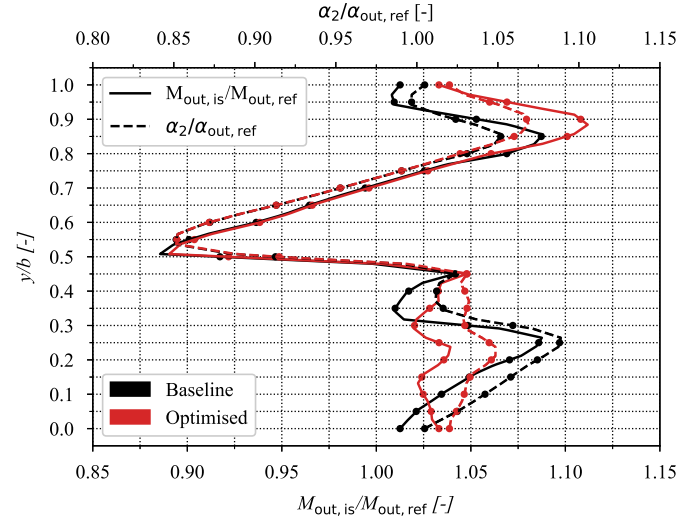

FIGURE 9: Span-wise Mach and flow angle distributions at the stator vane outlet. The reference value represents the mean outlet flow angle of the baseline design.

dynamic losses typical of supersonic impulse wheels. In this study, the flow uniformity parameter was quantified as the area-weighted standard mean deviation of the pitchwise pressure at the stator outlet boundary.

Figure 4 shows the evolution of the flow uniformity parameter over the optimisation history. It can be observed that the trend of the flow uniformity parameter is similar to that of the entropy generation loss coefficient and that the both quantities are reduced by the same order of magnitude.

Figure 9 shows the pitchwise distribution of the outlet Mach number and flow angle for the baseline and the optimised stator blade. The optimisation led to a 4.0% decrease in the value of standard deviation of the outlet flow angle and an increase of 0.8% in the standard deviation value the outlet Mach number. Given that the rotor efficiency is highly affected by the incoming flow-uniformity, its decrease is expected to be beneficial for the fluid-dynamic performance of the turbine.

4.1.3 Loss Breakdown
A loss breakdown was carried out to gain quantitative insight of the share in the loss contribution mechanisms of the baseline and the optimized geometry. The variation of the loss components over the optimisation history is illustrated in Figure 10. The total loss is reduced by 5.93%, which can be attributed to a reduction of the boundary layer loss by 0.85%, a reduction of the shockwave loss by 5.90% and an increase of the trailing edge loss by 0.83%. As previously anticipated by the contour plot, the mechanism mainly contributing to the overall loss reduction is the attenuation of shock loss.
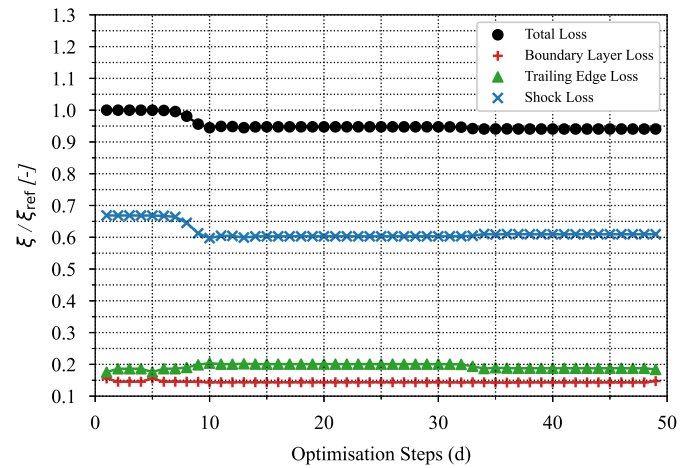

FIGURE 10: Variation of the loss components with the optimisation design steps. The reference loss coefficient is the total loss coefficient calculated at the first design step.

4.2 Part-Load Conditions
The rocket engine turbine is supplied with hot gases from the combustion chamber through a turbine inlet manifold. The primary function of the inlet manifold is to evenly distribute the hot gases among the stator vanes, however, this never occurs in practice. Therefore, the resulting circumferential non-uniformity leads the vanes to operate at pressure ratio slight different than that at nominal conditions. To study the impact that the optimized design has on such part-load operations, the fluid dynamic performance of the vane is computed by varying the pressure ra-
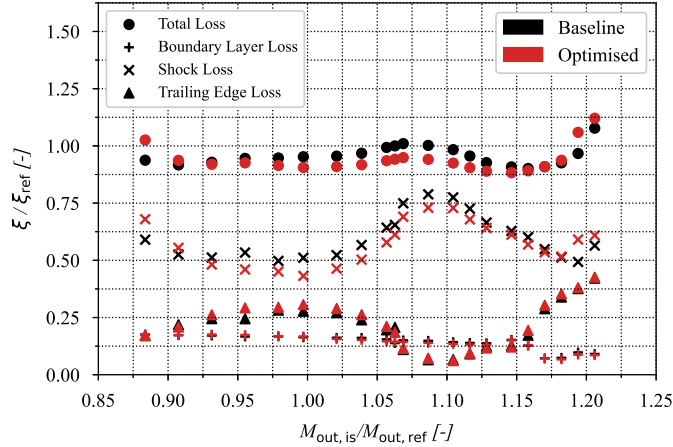
FIGURE 11: Variation of the energy loss coefficients ξ with isentropic exit Mach number $M_{out,is}$ for the baseline and optimised stator vane. The reference loss coefficient represents the total loss coefficient of the baseline design under nominal operating conditions of $M_{out,is}/M_{out,ref} = 1.06$. The reference Mach number represents the average target value for the outlet Mach number.

tio across the stator in the range -31%, +56% with respect to the nominal conditions. The envelope was chosen so as to consider variation in the pressure ratio in order of 30%. Since, supersonic flow regime is more interesting in terms of loss generation, the pressure ratio envelope was extended towards the higher pressure ratio. In this study, this change in pressure ratio was obtained by varying the static back-pressure. In the following, the isentropic Mach number ($M_{out,is}$) corresponding to a given back-pressure is used for comparison.

4.2.1 Flow Field Figure 11 illustrates the total loss in the stator vane at different outlet isentropic Mach number ($M_{out,is}$). It can be noted that when operating at off-design condition the fluid dynamic performance does not substantially decay compared to their nominal value. Previous study on converging-diverging supersonic vanes showcased a more rapid decay of fluid-dynamic performance at part-load. In addition, it can also be observed that the optimized geometry performs better than the baseline geometry for a range of conditions in the operating envelope, more precisely for $0.93 < M_{out,is}/M_{ref} < 1.17$. However, beyond these limits the performance of the optimised stator vane deteriorate more than those of the baseline geometry. This performance drop can be mainly attributed to the increase of shock losses, see Figure 11.

To identify the most relevant flow features, e.g. the shock wave structure and shock-wave boundary layer interaction, at part load conditions, the density gradient contours for five different pressure ratios are plotted in Figure 12. Specifically, the contours of the two most extreme cases, $M_{out,is}/M_{ref}$ of 0.88 and

1.19, the point where the performance of the baseline and optimized geometry overlap, $M_{out,is}/M_{ref}$ of 0.98, the design point, $M_{out,is}/M_{ref}$ of 1.06 and the condition featuring a peak of losses close to the nominal condition, $M_{out,is}/M_{ref}$ of 1.09 are illustrated in Figure 12. The contours on the top correspond to the baseline geometry whereas those in the bottom correspond to the optimised geometry, with increasing pressure ratio from left to right. In both the geometries, it can be observed that the shock impinging on the suction side moves downstream as the stage pressure ratio increases. Furthermore, as the pressure ratio becomes higher the angle of the resulting fish-tail shock structure diminishes, see Figure 12 from left to right.

The contours for the condition $M_{out,is}/M_{ref} = 0.88$, namely the operational point characterized by the lowest expansion ratio, evidence that the shockwave reflecting onto the suction side of the optimized geometry is of higher intensity than that of the baseline geometry. The formation of such a strong shock is induced by the concave surface created by the optimisation process between y/c of 0.4-1.0 in Figure 5. The concavity of the profile has the net effect of imparting a higher deceleration to the flow, which can only occur if the flow passes through a shock of higher strength. This in-turn leads to the decay in the fluid dynamic performance and to a higher value of the non-uniformity parameter at the exit of the stator. The increase in shock loss can also be seen in Figure 11.

The contours of the case $M_{out,is}/M_{ref}$ corresponding to 1.19 are those of the point of the operational envelope characterized by the highest pressure ratio, see Figure 11. The characteristic shockwave pattern is significantly different in this case when compared to other lower pressure ratio cases. In this case the suction side is almost shock-free, except in the rear part where the shock originated from the trailing-edge impinges onto the wall, causing a boundary layer detachment. A similar pattern is observed for the optimized geometry, albeit the shock-boundary layer interaction occurs further downstream compared to the baseline geometry. From a quantitative point of view, the fluid-dynamic performance of the cascades at this severe operating condition are nearly coincident.

The contours for the case $M_{out,is}/M_{ref}$ equal to 0.98, namely the left crossing point in Figure 11, are characterised by a similar shockwave pattern. The only appreciable difference can be detected if looking at the reflection angle of the shockwave. The steeper shock wave observable in the contour of the optimized geometry is due to the more pronounced concavity of the suction surface close to the location of the shockwave impingement. It can be additionally seen that the shockwave strength remains comparable and so does the overall performance values for both the geometries. Nonetheless, the change of the shockwave angle has an effect, albeit minor, on the flow uniformity, as shown in Figure Figure 13.

The contours of $M_{out,is}/M_{ref}$ equal to 1.09, namely the operation condition characterized by a loss peak in Figure 11 show
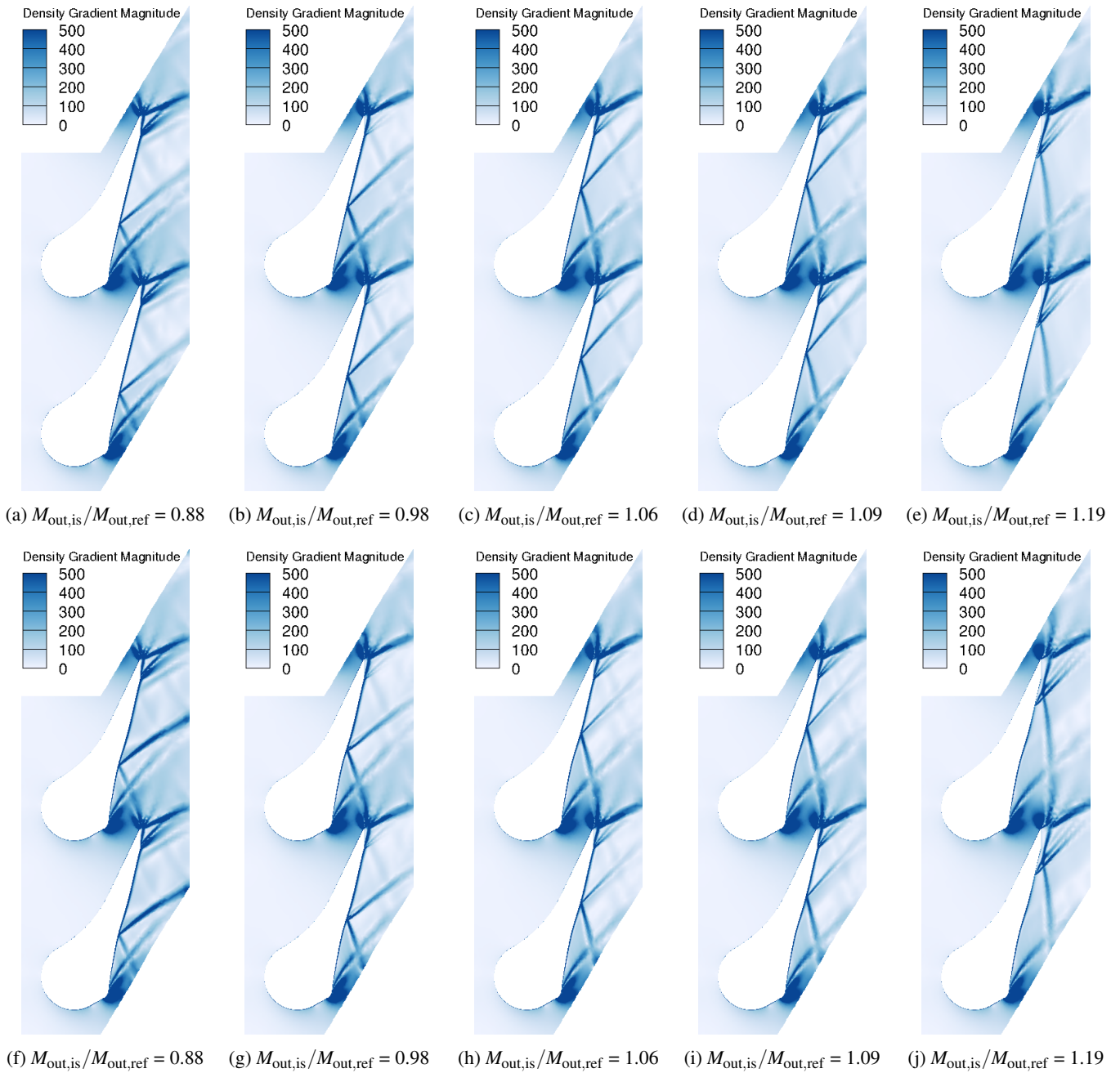
(a) $M_{out,is}/M_{out,ref} = 0.88$ (b) $M_{out,is}/M_{out,ref} = 0.98$ (c) $M_{out,is}/M_{out,ref} = 1.06$ (d) $M_{out,is}/M_{out,ref} = 1.09$ (e) $M_{out,is}/M_{out,ref} = 1.19$

(f) $M_{out,is}/M_{out,ref} = 0.88$ (g) $M_{out,is}/M_{out,ref} = 0.98$ (h) $M_{out,is}/M_{out,ref} = 1.06$ (i) $M_{out,is}/M_{out,ref} = 1.09$ (j) $M_{out,is}/M_{out,ref} = 1.19$

FIGURE 12: Density gradient magnitude contours of the baseline (top) and optimised (bottom) stator vane for nominal and off-nominal operating conditions, with increasing pressure ratio from left to right.

very similar flow features for the two geometries. The main difference that can be noticed is the weaker shock wave reflected from the suction side of the optimized supersonic vane. This is confirmed by examining the loss trend reported in Figure 11.

4.2.2 Flow Non-Uniformity The variation of the area-weighted standard deviation of the pitchwise outlet pressure as function of the isentropic exit Mach number is displayed in Figure 13. It can be inferred that a more uniform pitchwise outlet pressure profile is achieved for the optimised stator vane for $M_{out,is}/M_{ref} > 1.00$, and the results suggest that this continues
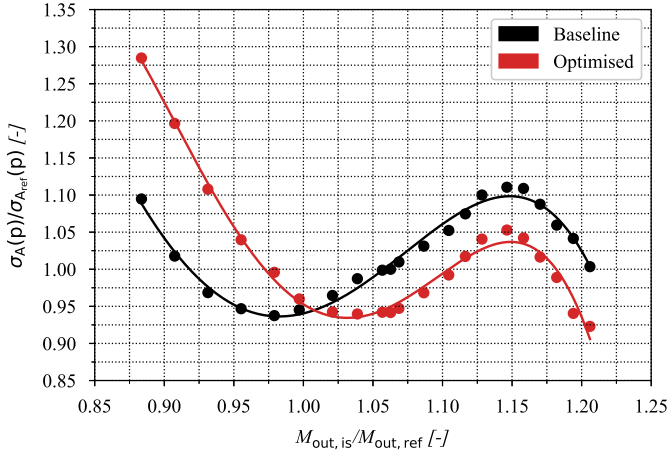
FIGURE 13: Variation of the outlet pressure non-uniformity parameter with the isentropic exit Mach number $M_{\text{out,is}}$ for the baseline and optimised stator vane. The reference $\sigma_A(p)$ is calculated for the baseline design under nominal operating conditions of $M_{\text{out,is}}/M_{\text{out,ref}} = 1.06$. The reference Mach number represents the average target value for the outlet Mach number.

for even higher $M_{\text{out,is}}$. Note that an improvement of the fluid dynamic performance of the vane does not necessarily translate into an enhancement of flow uniformity.

5 Conclusions

The present work documents the application of an adjoint based shape optimisation method to re-design a highly constrained supersonic stator vanes of a rocket engine turbine. The study considered the two-dimensional supersonic stator vanes of a 1MN-class gas generator cycle type rocket engine. The fluid dynamic performance of the cascade was assessed at both nominal and off-design conditions.

Based on the results presented in this study, the following conclusions can be drawn

1. Approximately 6% reduction of the entropy generation loss coefficient at nominal conditions was achieved by just deforming the suction side. The largest share of loss reduction is due to the mitigation of shock loss.
2. A reduction of the entropy generation coefficient does not necessarily entail an enhancement of flow uniformity. Therefore, the optimisation of supersonic stators should concurrently consider the minimization of both the loss coefficient and the flow uniformity parameter.
3. A single point optimisation does not guarantee improvement of the fluid-dynamic performance in the entire operational envelope of the vane. A multi-point optimisation method should therefore be adopted.

Future work will explore the potential of constrained optimization as well as the impact of stator-rotor interaction effects on the optimal shape of the stator. Multi-objective and multi-point adjoint-based optimisation methods will also be developed and applied to the case at hand.

References

[1] Douglas, H. W., 1974. "Turbopump systems for liquid rocket engines". *National Aeronautics and Space Administration (NASA)*(NASA-SP-8107).

[2] Ohlsson, G. O., 1964. "Supersonic turbines". *Journal of Engineering for Gas Turbine and Power,* **1**(86), pp. 7–12.

[3] Paniagua, G., Iorio, M., Vinha, N., and Sousa, J., 2014. "Design and analysis of pioneering high supersonic axial turbines". *International Journal of Mechanical Sciences,* **89**, pp. 65 – 77.

[4] Anand, N., Vitale, S., Pini, M., Otero, G. J., and Pecnik, R., 2019. "Design methodology for supersonic radial vanes operating in nonideal flow conditions". *Journal of Engineering for Gas Turbines and Power,* **141**(2), p. 022601.

[5] Harinck, J., Pasquale, D., Pecnik, R., van Buijtenen, J., and Colonna, P., 2013. "Performance improvement of a radial organic rankine cycle turbine by means of automated computational fluid dynamic design". *Proceedings of the Institution of Mechanical Engineers, Part A: Journal of Power and Energy,* **227**(6), pp. 637–645.

[6] Vitale, S., Albring, T. A., Pini, M., Gauger, N. R., and Colonna, P., 2017. "Fully turbulent discrete adjoint solver for non-ideal compressible flow applications". *Journal of the Global Power and Propulsion Society,* **1**.

[7] Razaaly, N., Persico, G., Gori, G., and Congedo, P. M., 2020. "Quantile-based robust optimization of a supersonic nozzle for organic rankine cycle turbines". *Applied Mathematical Modelling,* **82**, pp. 802 – 824.

[8] Bufi, E. A., Camporeale, S. M., and Cinnella, P., 2017. "Robust optimization of an organic rankine cycle for heavy duty engine waste heat recovery". *Energy Procedia,* **129**, pp. 66 – 73. 4th International Seminar on ORC Power SystemsSeptember 13-15th 2017.

[9] Sanghera, B. S., 2020. "Adjoint shape optimisation of rocket engine turbine blades". *TU Delft Research Repository* (Master Thesis Report).

[10] Anand, N., Vitale, S., Colonna, P., and Pini, M., 2018. "Assessment of FFD and CAD-based shape parametrization methods for adjoint-based turbomachinery shape optimization.". *In Proceeding of Global Propulsion and Power Conference, Montreal, Canada,*, p. 9.

[11] Paniagua, G., and Steelant, J., 2007. "Advances on propulsion technology for high-speed aircraft. volume 1". *Lecture Series: von Karman Institute for Fluid Dynamics*.

[12] Sederberg, T. W., and Parry, S. R., 1986. "Free-form defor-

mation of solid geometric models". In Proceedings of the 13th annual conference on Computer graphics and interactive techniques, pp. 151–160.

[13] Dwight, R. P. "Robust mesh deformation using the linear elasticity equations". In Computational Fluid Dynamics 2006, H. Deconinck and E. Dick, eds., Springer, pp. 401–406.

[14] Vitale, S., 2018. "Advancements in automated design methods for nicfd turbomachinery". PhD thesis, Delft University of Technology.

[15] Sagebaum, M., Albring, T., and Gauger, N. R. "Codipack code differentiation package – scientific computing.". *www.scicomp.uni-kl.de*.

[16] Griewank, A., and Walther, A., 2008. *Evaluating derivatives: principles and techniques of algorithmic differentiation.* SIAM.

[17] Mee, D. J., Baines, N. C., Oldfield, M. L. G., and Dickens, T. E. "An examination of the contributions to loss on a transonic turbine blade in cascade". pp. 155–162.

[18] Ghidoni, A., Pelizzari, E., Rebay, S., and Selmin, V., 2006. "3d anisotropic unstructured grid generation". *International journal for numerical methods in fluids,* **51**(9-10), pp. 1097–1115.

[19] Economon, D. T., Palacios, F., Copeland, S. R., Lukaczyk, T. W., and Alonso, J. J., 2015. "SU2: An open-source suite for multiphysics simulation and design.". *AIAA Journal,* **54**(3), pp. 828–846.

[20] Menter, F. R., 1994. "Two-equation eddy-viscosity turbulence models for engineering applications". *AIAA Journal,* **32**(8), pp. 1598–1605.

[21] Giles, M. B. "Nonreflecting boundary conditions for euler equation calculations". pp. 2050–2058.

[22] Roe, P. L., 1981. "Approximate riemann solvers, parameter vectors, and difference schemes". *Journal of computational physics,* **43**(2), pp. 357–372.

[23] Van Albada, G. D., Van Leer, B., and Roberts, W., 1997. "A comparative study of computational methods in cosmic gas dynamics". In *Upwind and high-resolution schemes.* Springer, pp. 95–103.

[24] Saad, Y., 1993. "A flexible inner-outer preconditioned gmres algorithm". *SIAM Journal on Scientific Computing,* **14**(2), pp. 461–469.

[25] Yoon, S., and Jameson, A., 1988. "Lower-upper symmetric-gauss-seidel method for the euler and navierstokes equations". *AIAA journal,* **26**(9), pp. 1025–1026.

[26] Souverein, L., Veggi, L., Sudhof, S., Behr, R., and Haidn, O., 2017. "On the effect of axial turbine rotor blade design on efficiency: a parametric study of the baljé-diagram". In European Conference for Aeronautics and Space Sciences.

[27] Saracoglu, B., Paniagua, G., Sanchez, J., and Rambaud, P., 2013. "Effects of blunt trailing edge flow discharge in supersonic regime". *Computers Fluids,* **88**, pp. 200 – 209.